



Pulsed Laser Deposition of Delafossite Oxide Thin Films on YSZ (001) Substrates as Solar Water Splitting Photocathodes

Journal:	Environmental Science: Nano		
Manuscript ID	EN-ART-08-2024-000706.R1		
Article Type:	Paper		

SCHOLARONE™ Manuscripts

Environmental Significance

This study investigates CuAlO₂ and CuFeO₂ thin film photocathodes for photoelectrochemical (PEC) water splitting, a sustainable method for converting solar energy into clean fuels. By exploring pulsed laser deposition to synthesize the delafossite phase of these materials, terminated by active Cu(I) sites, we aim to simplify the catalyst design, eliminating the need for complex heterostructures with protective layers and cocatalysts. Our measurements show notable PEC activities for both CuAlO₂ and CuFeO₂. Through combined synthesis, characterization, electrochemical measurements, and modeling, this work addresses the need to advance Cu(I) electrocatalysts. Our findings advance PEC systems, promoting renewable energy storage and reducing carbon emissions.

Pulsed Laser Deposition of Delafossite Oxide Thin Films on YSZ (001) Substrates as Solar Water Splitting Photocathodes

Chenyu Zhou¹, Atiya Banerjee¹, Esteban Luis Fornero², Zhaoyi Xi^{1,3}, Xiao Tong,¹ Eli Stavitski⁴, Xiaohui Qu^{1,*}, Sara E. Mason^{1,*}, Dario J. Stacchiola^{1,*}, Mingzhao Liu^{1,*}

¹Center for Functional Nanomaterials, Brookhaven National Laboratory, Upton, New York 11973, United States

² Instituto de Desarrollo Tecnológico para la Industria Química, UNL-CONICET, Güemes 3450, 3000 Santa Fe, Argentina

³Department of Materials Science and Chemical Engineering, Stony Brook University, Stony Brook, New York 11794, United States

⁴National Synchrotron Light Source II, Brookhaven National Laboratory, Upton, New York 11973, United States

Abstract

Development of solar energy converters with earth-abundant and environmentally friendly materials is one of the key routes explored towards a sustainable future. In this work, crystalline delafossite-phase CuAlO₂ and CuFeO₂ thin film solar water splitting photocathodes were fabricated using pulsed laser deposition. It was found that the desired delafossite phase was formed only after high temperature annealing in an oxygen-free atmosphere. The homogeneous delafossite bulk structure of the films was determined by correlating simulation results from first-principles calculations with synchrotron-based X-ray absorption near edge structure (XANES) spectroscopy. Both CuAlO₂ and CuFeO₂ photocathodes are active for solar water splitting, with the latter more efficient due to its narrower band gap and improved light absorption.

Introduction

In recent decades, Cu(I)-based delafossite oxide materials have emerged as prominent candidates in diverse technological applications, mainly embodying distinct yet related roles: transparent conducting oxides¹⁻³ and solar energy converter such as photoelectrodes for solar cell⁴⁻⁶, solar hydrogen evolution⁷⁻¹¹, and CO₂ conversion^{12, 13}. Their unique crystal structures, exceptional electronic properties, and promising electrochemical behavior have spurred extensive research efforts aimed at harnessing their potential for renewable energy, optoelectronics, and beyond. An important family of delafossite-type oxides are formulated as CuMO₂ (M = Al, Fe, Cr, Ga, etc) compounds, where Cu and M have oxidation states of +1 and +3, respectively.¹¹ Characterized by a layered arrangement featuring linearly coordinated Cu⁺ cations and layers of MO₆ octahedra that share edges, delafossite oxide typically adopt a rhombohedral $R\overline{3}m$ structure with trigonal symmetry (Figure 1a).

A wide range of deposition techniques have been reported to synthesize CuMO₂ films, including sol-gel^{14, 15}, hydrothermal¹⁶⁻¹⁸, chemical spray pyrolysis¹⁹, chemical vapor deposition (CVD)^{20, 21}, sputtering^{22, 23}, and pulsed laser deposition (PLD)²⁴⁻³⁰. The last one is particularly attractive due to its capacity to transfer stoichiometry from target material to thin film. Prior research endeavors concerning PLD-grown delafossite materials are summarized in Table 1. In order to maintain Cu in its optimally active intermediate oxidation state of +1, the chemical potential of oxygen must be carefully controlled during delafossite synthesis and post-growth annealing at higher temperature is usually needed. As illustrated by the Ellingham diagram of CuAlO₂, higher temperature will indeed stabilize the desired delafossite phase in an atmosphere of moderate oxygen partial pressure (Figure 1b).

In addition, most delafossite growth efforts have been concentrated on substrates exhibiting trigonal or hexagonal symmetry, such as sapphire.^{1, 24-33} Nonetheless, the insulating nature of sapphire poses challenges for applications necessitating high conductivity, such as photoelectrodes. Therefore, investigations in the realm of delafossite-based photovoltaic and photoelectrochemical research predominantly rely on fluorine-doped tin oxide (FTO) glass substrates, chosen for their transparency to light and efficient charge carrier transport.^{5, 7, 34-37} There are very few studies on other single crystalline substrate, such as yttrium-stabilized zirconia (YSZ), which has the advantage of being lattice-matched to indium tin oxide (ITO), a compelling alternative to FTO. Previously, we have demonstrated that epitaxial ITO layer can be grown on YSZ (001) for the fabrication of bismuth vanadate (BiVO₄) photoanodes.³⁸ However, to our knowledge, there is no previous studies on delafossite growth on this commonly available substrate.

In this work, we used PLD to fabricate CuAlO₂ and CuFeO₂ delafossite thin film photocathodes on ITO/YSZ (001) substrates and studied their solar water splitting activity in a photoelectrochemical cell as an example of their potential as energy converters. The structural properties of the deposited films were studied by thin film X-ray diffraction (XRD) and synchrotron-based X-ray absorption near edge structure (XANES) spectroscopy, demonstrating the growth of *c*-oriented single-phase delafossite thin films on YSZ (001) substrates. First-principles calculations of the XANES spectra confirmed that the thin films have atomic motifs matching the bulk structure.

Results and Discussion

Delafossite thin films were prepared by pulsed laser deposition (PLD) on (001)-oriented yttrium-stabilized zirconia (YSZ) substrates, which were first coated with a thin layer of indium tin oxide (ITO) for electrical conductivity. According to its X-ray diffraction (XRD) pattern, the

as-grown Cu-Al oxide thin film did not show any peaks corresponding to the delafossite phase, or any phases other than those in the ITO/YSZ substrate (Figure 2a), which suggests that the asgrown Cu-Al oxide film was amorphous. Similarly, the XRD pattern of as-grown Cu-Fe oxide film did not contain any delafossite peaks, but showed the presence of the spinel phase of CuFe₂O₄ (Figure 2b). According to the Ellingham diagram of the Cu-Fe-O system (Supporting Information, Figure S1), the delafossite CuFeO₂ is thermodynamically favored in a region with lower chemical potential of oxygen and higher temperature, while CuFe₂O₄ is stabilized in an oxygen-rich environment and at lower temperature.³⁹ The observation suggests that the PLD chamber does not have an O₂ partial pressure that is low enough to drive the CuFe₂O₄/CuFeO₂ equilibrium in the favor of the latter.

To drive phase equilibrium toward the desired delafossite phase and to promote its crystallization, the thin film of Cu-Al and Cu-Fe oxides are processed by post-growth annealing at 900 °C in nitrogen. In the case of Cu-Al oxide, a single peak emerged at 15.78°, attributed to the CuAlO₂ (003) plane, while the CuAlO₂ (006) peak overlapped with the K_{β} peak of YSZ (002) (Figure 2a). This observation indicates the formation of a c-oriented single-phase CuAlO₂ structure. In the case of Cu-Fe oxide, we observe the (003), (006), and (009) diffraction peaks of CuFeO₂, respectively at 15.48°, 31.26°, and 47.68° (Figure 2b). Because there was no epitaxial relationship between delafossite and the ITO/YSZ (001) substrate, the formation of delafossite phase required more strict control of conditions. We note that when the substrate is replaced with c-plane sapphire, c-axis oriented single-phase CuFeO₂ was formed during PLD at the same deposition conditions (700°C, 2 × 10⁻² mbar N₂ atmosphere), without the requirement of post-growth annealing (Supporting Information, Figure S2a). Interestingly, the delafossite CuFeO₂ phase can still form on sapphire even after a small amount of oxygen was introduced. As shown in Supporting

Information Figure S2b, both delafossite $CuFeO_2$ and spinel $CuFe_2O_4$ phases can be identified from the XRD pattern of the Cu-Fe oxide film grown in 1 mTorr O_2 (1.3 × 10⁻⁶ bar). This clearly reflects that a metastable thin film phase can be stabilized by reducing its surface energy through lattice matching to the substrate.

Although XRD confirmed the formation of delafossite phases of $CuAlO_2$ and $CuFeO_2$, in which Cu takes a formal oxidation number of +1, X-ray photoelectron spectroscopy (XPS) found that the surface of delafossite film was dominated by Cu +2 species. This was evident by the emergence of strong satellite peaks in the Cu 2p XPS spectra (Figures 3a and 3c), which would be very weak if Cu had oxidation state of 0 or +1. Since XPS is a surface-sensitive technique, the observation suggested that the surface of delafossite films was oxidized upon air exposure. The Al 2p peak of $CuAlO_2$ was consistent with Al with oxidation state +3 and overlapped with the broader Cu 3p_{3/2} peak (Figure 3b). The Fe 2p region of $CuFeO_2$ must be fitted with two sets of $2p_{3/2} - 2p_{1/2}$ doublets, in addition to a pair of satellite peaks (Figure 3d). However, this does not indicate the presence of Fe +2 species, since the lowest binding energy of Fe $2p_{3/2}$ remains at 710 eV, while Fe +2 would have Fe $2p_{3/2}$ binding energy at 709 eV. This is similar as the case of Fe_2O_3 , which requires multiple sets of peaks to properly fit the Fe 2p features.⁴⁰

Nevertheless, X-ray absorption near edge structures (XANES) spectroscopy, a bulk-sensitive technique, confirmed that the bulk of the films remained delafossite despite the surface oxidation. A unique feature of delafossite lattice ($A^+B^{3+}O_2$, space group $R\overline{3}m$) is that the A^+ cations are linearly coordinated and have a coordination number (C.N.) of 2, while the B^{3+} cations occupy octahedral sites (C.N. = 6). This contrasts with the caswellsilverite lattice of $A^+B^{3+}O_2$, which is also in the space group $R\overline{3}m$, but has A^+ and B^{3+} cations both occupying octahedral sites. The linear coordination of Cu^+ in our $CuAlO_2$ and $CuFeO_2$ films are confirmed by their XANES spectra

at Cu K-edge (Figure 4a). In both cases, the spectrum is characterized by a sharp shoulder feature that peaks at 8981 eV. This feature is consistent with the linear coordination of Cu⁺ cations and is similarly observed in Cu₂O⁴¹, in which each Cu⁺ ion is linearly coordinated with two O²⁻ ions. According to Kau et al, this feature may be identified as the electric dipole-allowed 1s \rightarrow 4p_{x,y} transition, which has a lower energy than the 1s \rightarrow 4p_z transition, due to the antibonding formation between Cu 4p_z and ligands (z is along the O-Cu-O axis).⁴² In general, the sharp feature at 8981 eV would disappear, if the Cu⁺ cation is located at a higher C.N. site, e.g., trigonal or tetrahedral.⁴¹

The qualitative analysis of the Cu K-edge XANES is confirmed by first-principles computation. The structure of the thin delafossite film was relaxed using the Perdew-Burke-Ernzerhof (PBE) functional with a slab atomic model and the XANES were simulated with multiple scattering theory using the FDMNES program package. 43 The simulated Cu⁺ K-edge spectra were quite similar between CuAlO₂ and CuFeO₂, with the characteristic pre-edge shoulder feature at 8981 eV observed clearly (Figure 4b). Compared with the experimental spectra, the simulated delafossite spectra not only preserved the sharp shoulder features at 8991 eV, but also very well reproduced the shape of the lower energy (and stronger) white line peak at about 8994 eV. Given that XPS found surface Cu atoms were oxidized to an oxidation number of +2, we also simulated the XANES spectra of Cu +2 species following the same approach. For these simulations, spinel CuAl₂O₄ and CuFe₂O₄ were respectively chosen as model compounds for the surface oxidation of CuAlO₂ and CuFeO₂. Their lattice structures were taken from the Materials Project, mp-27719 for spinel CuAl₂O₄ and mp-770107 for CuFe₂O₄. As shown in Figure 4c, the simulated Cu K-edge spectra of CuAl₂O₄ and CuFe₂O₄ showed little similarity with the experimental spectra. The preedge shoulder was much weaker than those experimentally observed for delafossite films and was moved to higher energy (8982 eV vs 8981 eV). As such, we may conclude that the PLD-grown

CuAlO₂ and CuFeO₂ films were dominated by the delafossite phase, despite the formation of small amount of Cu +2 species due to surface oxidation.

The photoelectrochemical (PEC) water reduction activities of both CuAlO₂ and CuFeO₂ thin films was evaluated using linear sweep voltammetry in a phosphate buffer solution at pH 7. Prior to the sweep, the dissolved O₂ in the electrolyte solution was purged thoroughly by bubbling argon gas. This step is crucial to ensure that photoelectrons participate in water reduction rather than O₂ reduction. In the PEC experiment, the illumination source is a Xenon arc lamp equipped with a filter to simulate AM 1.5 G solar radiation. As depicted in Figures 5a and 5b, both CuAlO2 and CuFeO₂ exhibit notable PEC activities upon illumination. However, CuFeO₂ exhibits photocurrent density at the potential of hydrogen evolution (0 V_{RHE}) that is one order of magnitude higher than that of CuAlO₂. This stark difference can be attributed to the significantly narrower optical bandgap of CuFeO₂ (2.0 eV vs. 3.5eV), 1, 44 which results in more efficient absorption of incident light and charge carrier generation. Despite the chemical stability of CuFeO₂, we note that its photocurrent density at 0 V_{RHE} (0.25 mA/cm²) remains much lower than the theoretical limit of a semiconductor with 2 eV band gap (about 15 mA/cm²) and the highest photocurrent density achieved by Cu₂O photocathode (about 10 mA cm⁻²). 45, 46 This suggests a low charge carrier separation efficiency that requires further study and optimization.

Mott-Schottky analysis, in which the space charge capacitance ($C_{\rm sc}$) is correlated with the electrode potential (E), was conducted to characterize the doping type and doping level of CuFeO₂. The $1/C_{\rm sc}^2 - E$ plot had a uniform negative slope about -0.03 μ F⁻² cm⁴ V⁻¹, which confirms the p-type doping of CuFeO₂ (Figure 5c). According to the Mott-Schottky relation, the slope is equal to $-2(e\epsilon\epsilon_0 N_{\rm A})^{-1}$, where e is the elementary charge, ϵ the semiconductor dielectric constant, ϵ_0 the

vacuum permittivity, and N_A the acceptor density. Given that bulk CuFeO₂ is ferroelectric with $\epsilon \sim 10^4$, we estimate that the CuFeO₂ had an acceptor density of about 5×10^{17} cm⁻³.

In summary, we used PLD to fabricate delafossite CuAlO₂ and CuFeO₂ photocathodes on ITO-buffered YSZ (001) substrates and compared their solar water splitting activities using photoelectrochemistry measurements. Although the delafossite phase can be readily formed on a lattice-matching sapphire substrate, the stabilization of delafossite on ITO/YSZ was more challenging and achieved only after post-growth high temperature annealing. Cu K-edge XANES largely matched the expectation for Cu⁺ occupying a linearly coordinated center, through a careful comparison with first-principles calculation results. To date, all known electrocatalysts for CO₂ reduction directly into high value C₂₊ products contain copper as the active site.⁴⁷⁻⁵⁰ As a Cu-containing p-type oxide that has a visible light optical gap, the activity of CuFeO₂ as a water splitting photocathode opens a door toward its application for the most desirable and challenging sustainable photoelectrochemical conversion reactions involving carbon dioxide.

Methods

Thin film synthesis

The ceramic targets for pulsed laser deposition (PLD) of Cu(I)-based delafossite were prepared via a solid-state sintering process. The CuO powder (Alfa Aesar) is mixed with the powder of trivalent metal oxide, either Al₂O₃ (Alfa Aesar) or Fe₂O₃ (Alfa Aesar), in a stoichiometric 1:1 ratio of the respective metal elements. The powder mixture was grounded in an agate mortar, pressed into pellets using a hydraulic pump at a pressure of 10 Ton, and subsequently sintered in air at 800 °C, for 10 hours. During the PLD process, a laser fluence of 1.8 J/cm² (KrF, 248 nm) and a repetition rate of 5 Hz were employed. Initially, a 50-nm thick layer of indium tin oxide (ITO) was

deposited onto an yttrium-stabilized zirconia (YSZ) substrate at 600° C in vacuum (with a base pressure of 6×10^{-7} mbar), as a conductive back contact for subsequent photoelectrochemical measurements. The deposition of Cu(I) delafossite took place at 700° C in a nitrogen atmosphere with a pressure of 2×10^{-2} mbar. Following the deposition process, the system was gradually cooled down to room temperature under the same oxygen pressure, at a rate of 10° C per minute. The deposited thin films were annealed in nitrogen at 900° C for 1 h.

Materials Characterization

The crystalline phases of thin film were characterized by X-ray diffraction (XRD, Rigaku SmartLab) using Cu K α radiation (λ = 1.5418 Å). X-ray photoelectron spectroscopy (XPS) measurements are performed in a high vacuum (~10-7 Torr) using Al K α (1486.6 eV) as the excitation source. X-ray absorption near edge structure (XANES) spectra at Cu K-edge are measured at the ISS beamline (8-ID)⁵¹ of NSLS-II, with the sample mounted in a similar fashion as for the XRF measurement. A fast scanning, liquid nitrogen cooled double crystal monochromator is used for continuous energy scans, with the energy range set to 8950 – 9200 eV. The X-ray absorption is determined by calculating the total fluorescence yield $\mu(E) = I_f/I_0$, where I_f is the fluorescence intensity and I_0 the incident intensity. The intensity of the incident beam is measured by an ion chamber, and the X-ray fluorescence from the sample is captured by a PIPS (Passivated Implanted Planar Silicon) detector. The spectroscopic scans are repeated multiple times with the same settings, then binned and averaged to reduce the noise.

Photoelectrochemical (PEC) measurements were carried out using a potentiostat (PAR VersaStat) in a three-electrode cell, with BVO thin film serving as the working electrode, Ag/AgCl as the reference electrode, and Pt wire as counter electrode. The simulated solar light was provided by a 150 W solar simulator equipped with an air mass 1.5 global (AM 1.5 G) filter (Newport) and

the light power was calibrated to 1 Sun (100 mW/cm²) using a quartz-windowed Si solar cell (Newport). The electrolyte was a pH 7 phosphate buffer solution. Before the voltametric scan, the dissolved oxygen in the electrolyte solution was purged thoroughly by argon bubbling. The argon gas purging was maintained through the PEC experiment in a flow rate that forms minimal bubble.

First-Principles Calculations

Electronic structure calculations of CuMO₂ (M = Al or Fe) were carried out using spin-polarized density functional theory as implemented in Quantum ESPRESSO⁵² using the generalized gradient approximation of Perdew, Burke, and Ernzerhof⁵³ and ultrasoft pseudopotentials⁵⁴. A plane-wave cutoff of 50 Ry and a charge density cutoff of 400 Ry were used, and all the atoms were fully relaxed during the geometry optimizations. The energy was sampled using k-point grids of $8\times8\times8$. The optimized lattice constants a and c were 2.88 (3.07) and 17.13 (17.06) Å for CuAlO₂ and CuFeO₂, respectively.

AUTHOR INFORMATION

Corresponding Author

* E-mail: xiaqu@bnl.gov;

* E-mail: smason@bnl.gov;

* E-mail: <u>djs@bnl.gov</u>;

* E-mail: <u>mzliu@bnl.gov</u>

Conflicts of interest

All authors have given approval to the final version of the manuscript. The authors declare no competing financial interest.

Acknowledgement

This research used Materials Synthesis & Characterization, Proximal Probes, and Theory & Computation facilities of the Center for Functional Nanomaterials (CFN), and the 8-ID (ISS) beamline of the National Synchrotron Light Source II (NSLS II), the U.S. Department of Energy Office of Science User Facilities, at Brookhaven National Laboratory under Contract No. DE-SC0012704.

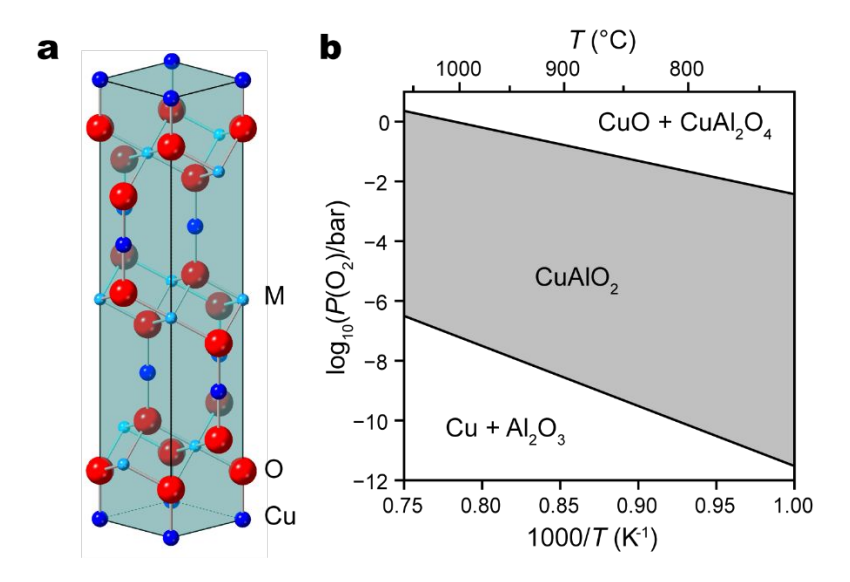


Figure 1. (a) Crystal structure and unit cell of delafossite $CuMO_2$ (M = Al, Fe, etc). A few atoms outside of the unit cell are included for better view of the coordination shell around M atoms. (b) Ellingham diagram of the Cu-Al-O system, with the atomic ratio Cu : Al = 1 : 1.

Table 1. A survey of literatures on PLD-grown delafossite thin film materials. (SA = sapphire; AG = amorphous glass; YSZ = yttrium stabilized zirconia).

Delafossite	Substrate	T (°C)a	P _{O2} (mTorr) ^a	Annealing	Crystal Phase	Ref
CuAlO ₂	SA (001)	700	100	-	c-axis oriented single phase (001) ^b	1
	SA (001)	100-200	100	1050°C, air, 1.5 h ^c	c-axis oriented single phase (00l)	24
	SA (001)	500	~20	900°C, N ₂ , 1 h	c-axis oriented single phase (00l)	25
	SA (001)	650	10	1100°C, air, 30 min	c-axis oriented single phase (00l)	26
	SA (001)	700	100	1050°C, air, 10 min	c-axis oriented single phase (00l)	27
CuFeO ₂	SA (001)	500	75	500°C, O ₂ , 10 min	Epitaxial single- phase (001) ^b	28
	SA (001)	600	0.1	-	c-axis oriented single phase (00l)	29
	SA (001)	600	0.1	-	c-axis oriented single phase (00l)	30
	AG	750	1	-	c-axis oriented single phase (00l)	55
	SA (001)	550-600	0.1	-	Epitaxial single- phase (001)	31
	SA (001)	850	0.5	-	Epitaxial single- phase (001)	32

- a. Listed are the temperature and pressure conditions for the optimal outcome.
- b. If the in-plane orientation of the thin film is tested to match rhombohedral crystal system, it is listed as epitaxial single-phase. If only the out-of-plane orientation is examined, it is listed as c-axis oriented single phase, otherwise.
- c. Mixed with CuO and Al₂O₃ powders in closed crucible.
- d. Annealing is only for smoothing the surface of thin film.

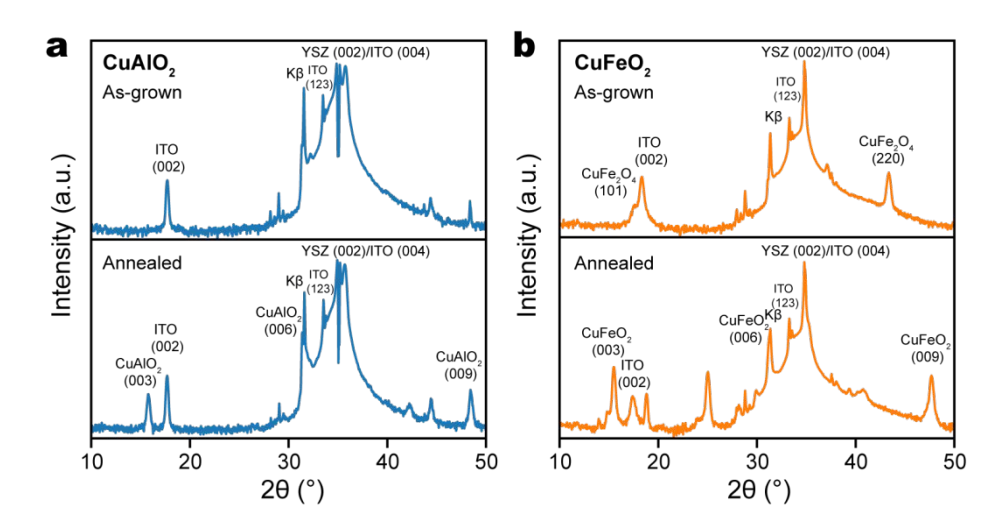


Figure 2. XRD patterns of (a) CuAlO₂/ITO/YSZ and (b) CuFeO₂/ITO/YSZ thin films, as-grown by PLD (top) and after annealing in N₂ at 900°C (bottom).

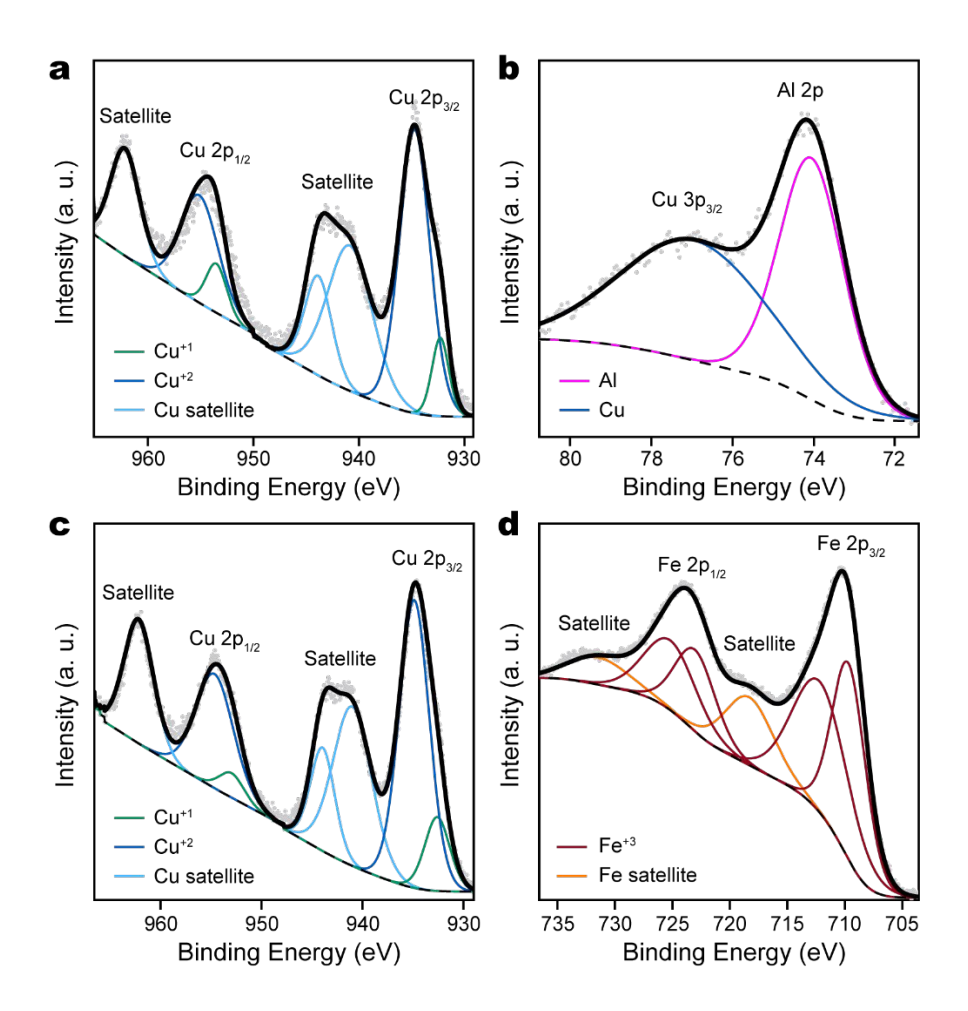


Figure 3. XPS spectra of CuAlO₂ thin films, in (a) Cu 2p region and (b) Al 2p region, and of CuFeO₂ thin films, in (c) Cu 2p region and (d) Fe 2p region, with corresponding spectral fitting. In each panel, the gray dots are experimental data, the solid black line is the fitted spectrum, and the dashed line is the fitted background.

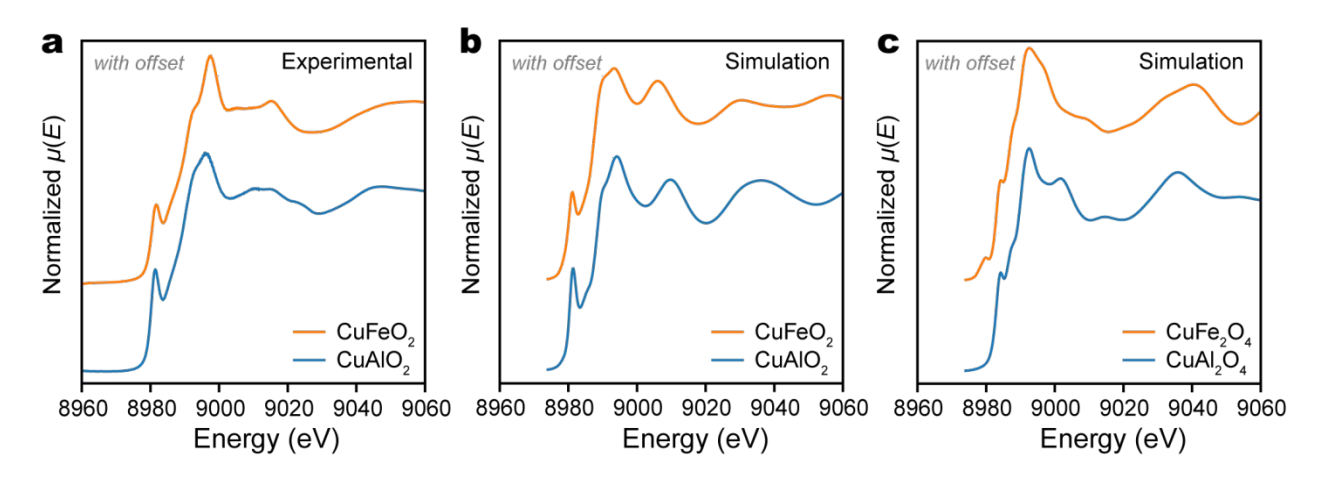


Figure 4. (a) Experimental Cu K-edge XANES spectra of delafossite $CuAlO_2$ and $CuFeO_2$ thin films. (b) Simulated Cu K-edge XANES spectra of delafossite $CuAlO_2$ and $CuFeO_2$, in which Cu takes a formal oxidation number of +1. (c) Simulated Cu K-edge XANES spectra of spinel $CuAl_2O_4$ and $CuFe_2O_4$, in which Cu takes a formal oxidation number of +2.

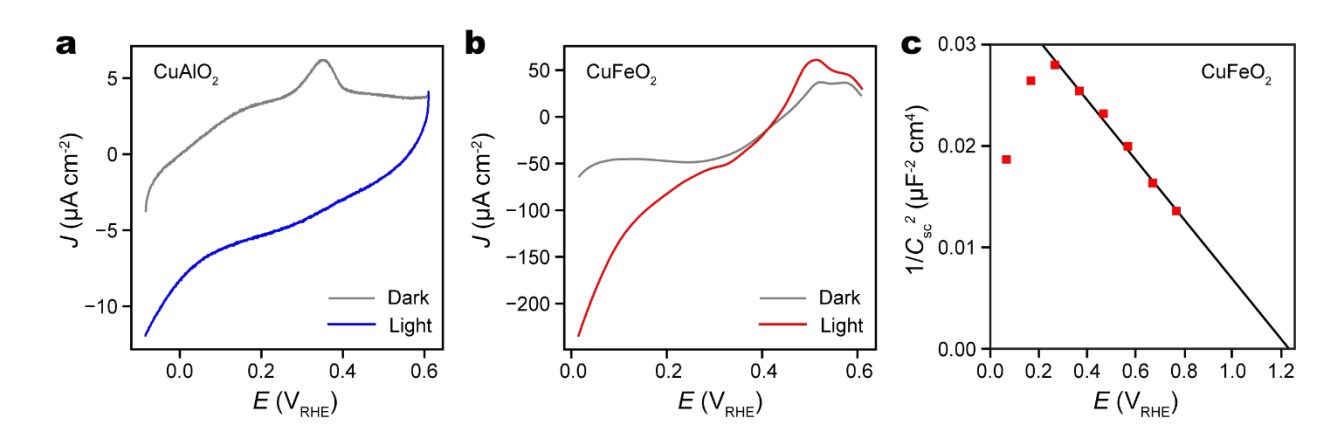


Figure 5. Photocurrent density (J) - potential (E) characteristics of (a) CuAlO₂/ITO/YSZ and (b) CuFeO₂/ITO/YSZ thin films. (c) Mott-Schottky plot of CuFeO₂/ITO/YSZ thin film. The red squares are experimental data and the black line is the fitting for the linear range (0.4 – 0.8 V_{RHE}).

References

- 1. Kawazoe, H.; Yasukawa, M.; Hyodo, H.; Kurita, M.; Yanagi, H.; Hosono, H., *Nature* **1997,** *389*, 939-942.
- 2. Banerjee, A. N.; Chattopadhyay, K. K., *Prog. Cryst. Growth Charact. Mater.* **2005,** *50*, 52-105.
- 3. Stadler, A., *Materials* **2012**, *5*, 661-683.
- 4. Yu, M. Z.; Draskovic, T. I.; Wu, Y. Y., Phys. Chem. Chem. Phys. **2014**, 16, 5026-5033.
- 5. Zhu, T., et al., J. Alloy Compd. **2016**, 685, 836-840.
- 6. Akin, S.; Sadegh, F.; Turan, S.; Sonmezoglu, S., *ACS Appl. Mater. Interfaces* **2019**, *11*, 45142-45149.
- 7. Read, C. G.; Park, Y.; Choi, K. S., J. Phys. Chem. Lett. **2012**, *3*, 1872-1876.
- 8. Sivula, K.; van de Krol, R., *Nat. Rev. Mater* **2016,** *I*, 15010.
- 9. Jang, Y. J.; Lee, J. S., Chemsuschem **2019**, *12*, 1835-1845.
- 10. Li, C. L.; He, J. F.; Xiao, Y. Q.; Li, Y. B.; Delaunay, J. J., *Energy Environ. Sci.* **2020,** *13*, 3269-3306.
- 11. Diez-Garcia, M. I.; Gomez, R., Sol. RRL **2022**, *6*, 2100871.
- 12. Baiano, C.; Schiavo, E.; Gerbaldi, C.; Bella, F.; Meligrana, G.; Talarico, G.; Maddalena, P.; Pavone, M.; Munoz-Garcia, A. B., *Mol. Catal.* **2020**, *496*, 111181.
- 13. Gu, J.; Wuttig, A.; Krizan, J. W.; Hu, Y. A.; Detweiler, Z. M.; Cava, R. J.; Bocarsly, A. B., *J. Phys. Chem. C* **2013**, *117*, 12415-12422.
- 14. Benreguia, N.; Barnabe, A.; Trari, M., *J. Sol-Gel Sci. Technol.* **2015,** *75*, 670-679.
- 15. Prevot, M. S.; Guijarro, N.; Sivula, K., Chemsuschem **2015**, 8, 1359-1367.
- 16. Sheets, W. C.; Mugnier, E.; Barnabe, A.; Marks, T. J.; Poeppelmeier, K. R., *Chem. Mater.* **2006**, *18*, 7-20.
- 17. Xiong, D. H.; Zeng, X. W.; Zhang, W. J.; Wang, H.; Zhao, X. J.; Chen, W.; Cheng, Y. B., *Inorg. Chem.* **2014**, *53*, 4106-4116.
- 18. Yu, M. Z.; Draskovic, T. I.; Wu, Y. Y., *Inorg. Chem.* **2014**, *53*, 5845-5851.
- 19. Garcia-Torregrosa, I.; Geertzema, Y. G.; Ismail, A. S. M.; Lee, T. L.; de Groot, F. M. F.; Weckhuysen, B. M., *Chemphotochem* **2019**, *3*, 1238-1245.
- 20. Yengantiwar, A.; Shinde, P. S.; Pan, S. L.; Gupta, A., *J. Electrochem. Soc.* **2018**, *165*, H831-H837.
- 21. Piza-Ruiz, P.; Saenz-Trevizo, A.; Verde-Gomez, Y.; Amezaga-Madrid, P.; Miki-Yoshida, M., *Ceram. Int.* **2019**, *45*, 1156-1162.
- 22. Tsuboi, N.; Takahashi, Y.; Kobayashi, S.; Shimizu, H.; Kato, K.; Kaneko, F., *J. Phys. Chem. Solids* **2003**, *64*, 1671-1674.
- 23. Barnabe, A.; Mugnier, E.; Presmanes, L.; Tailhades, P., *Mater. Lett.* **2006,** *60*, 3468-3470.
- 24. Stauber, R. E.; Perkins, J. D.; Parilla, P. A.; Ginley, D. S., *Electrochem. Solid-State Lett.* **1999,** *2*, 654-656.
- 25. Deng, Z. H.; Fang, X. D.; Tao, R. H.; Dong, W. W.; Li, D.; Zhu, X. B., *J. Alloy Compd.* **2008**, *466*, 408-411.
- 26. Lee, J. C.; Um, S. Y.; Heo, Y. W.; Lee, J. H.; Kim, J. J., *J. Eur. Ceram. Soc.* **2010,** *30*, 509-512.
- 27. Neumann-Spallart, M.; Pai, S. P.; Pinto, R., *Thin Solid Films* **2007**, *515*, 8641-8644.

- 28. Li, S. Z.; Liu, J.; Wang, X. Z.; Yan, B. W.; Li, H.; Liu, J. M., *Physica B* **2012**, *407*, 2412-2415.
- 29. Wheatley, R. A.; Rojas, S.; Oppolzer, C.; Joshi, T.; Borisov, P.; Lederman, D.; Cabrera, A. L., *Thin Solid Films* **2017**, *626*, 110-116.
- 30. Vojkovic, S.; Fernandez, J.; Elgueta, S.; Vega, F. E.; Rojas, S. D.; Wheatley, R. A.; Seifert, B.; Wallentowitz, S.; Cabrera, A. L., *SN Appl. Sci.* **2019**, *1*, 1322.
- 31. Joshi, T., et al., J. Appl. Phys. **2015**, 117, 013908.
- 32. Luo, S. J., et al., J. Appl. Phys. **2020**, 127, 065301.
- 33. Ueda, K.; Hase, T.; Yanagi, H.; Kawazoe, H.; Hosono, H.; Ohta, H.; Orita, M.; Hirano, M., *J. Appl. Phys.* **2001,** *89*, 1790-1793.
- 34. Choi, S. Y.; Kim, C. D.; Han, D. S.; Park, H., J. Mater. Chem. A 2017, 5, 10165-10172.
- 35. Miclau, M.; Miclau, N.; Banica, R.; Ursu, D., *Mater. Today Proc.* **2017**, *4*, 6975-6981.
- 36. Prevot, M. S.; Li, Y.; Guijarro, N.; Sivula, K., J. Mater. Chem. A 2016, 4, 3018-3026.
- 37. Prevot, M. S.; Jeanbourquin, X. A.; Bouree, W. S.; Abdi, F.; Friedrich, D.; van de Krol, R.; Guijarro, N.; Le Formal, F.; Sivula, K., *Chem. Mater.* **2017**, *29*, 4952-4962.
- 38. Zhang, W., et al., Chem. Mater. 2018, 30, 1677-1685.
- 39. Stöcker, T.; Moos, R., *Materials* **2018,** *11*, 1888.
- 40. Biesinger, M. C.; Payne, B. P.; Grosvenor, A. P.; Lau, L. W. M.; Gerson, A. R.; Smart, R. S. C., *Appl. Surf. Sci.* **2011**, *257*, 2717-2730.
- 41. Guda, A. A., et al., npj Comput. Mater. 2021, 7, 203.
- 42. Kau, L. S.; Spira-Solomon, D. J.; Penner-Hahn, J. E.; Hodgson, K. O.; Solomon, E. I., *J. Am. Chem. Soc.* **1987**, *109*, 6433-6442.
- 43. Bunău, O.; Joly, Y., J. Phys. Condens. Matter **2009**, 21, 345501.
- 44. Galakhov, V. R.; Poteryaev, A. I.; Kurmaev, E. Z.; Anisimov, V. I.; Bartkowski, S.;
- Neumann, M.; Lu, Z. W.; Klein, B. M.; Zhao, T.-R., Phys. Rev. B 1997, 56, 4584-4591.
- 45. Cheng, J.; Wu, L.; Luo, J., Chem. Phys. Rev. 2022, 3, 031306
- 46. Tilley, S. D., ACS Energy Lett. 2023, 8, 2338-2344.
 47. Long, C., et al., Sci. Adv. 2023, 9, eadi6119.
- 48. Liu, W., et al., Nat. Commun. 2022, 13, 1877.
- 49. Li, X., et al., Chem **2022**, 8, 2148-2162.
- 50. Jun, M.; Kundu, J.; Kim, D. H.; Kim, M.; Kim, D.; Lee, K.; Choi, S.-I., *Adv. Mater.* **2024,** *36*, 2313028.
- 51. Leshchev, D.; Rakitin, M.; Luvizotto, B.; Kadyrov, R.; Ravel, B.; Attenkofer, K.; Stavitski, E., *J. Synchrotron Radiat.* **2022**, *29*, 1095-1106.
- 52. Giannozzi, P., et al., J. Phys. Condens. Matter 2017, 29, 465901.
- 53. Perdew, J. P.; Burke, K.; Ernzerhof, M., *Phys. Rev. Lett.* **1996,** 77, 3865-3868.
- 54. Garrity, K. F.; Bennett, J. W.; Rabe, K. M.; Vanderbilt, D., *Comput. Mater. Sci.* **2014**, *81*, 446-452.
- 55. Choi, D. H.; Moon, S. J.; Hong, J. S.; An, S. Y.; Shim, I. B.; Kim, C. S., *Thin Solid Films* **2009**, *517*, 3987-3989.

Data availability

All data supporting the findings of this study are presented in the main article and the ESI.